Journal of Materials Chemistry C

Accepted Manuscript

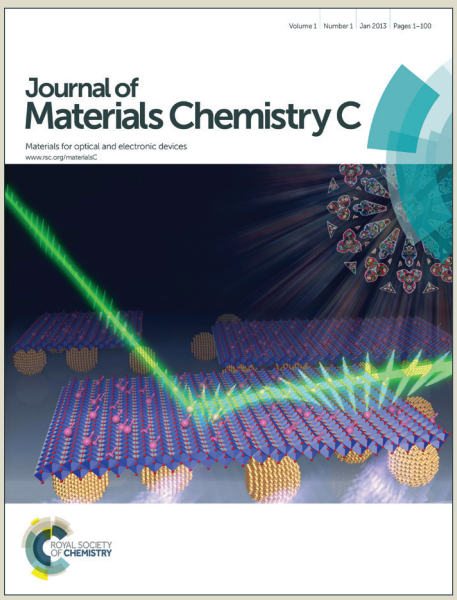

ROYAL SOCIETY OF CHEMISTRY

www.rsc.org/materialsC

Journal of Materials Chemistry C

RSCPublishing

ARTICLE

Impact of titanium content and postdeposition annealing on the structural and sensing properties of $TbTi_xO_y$ sensing membranes

Cite this: DOI: 10.1039/x0xx00000x

Received 18th April 2014,
Accepted XXth XXX 2014

DOI: 10.1039/x0xx00000x

www.rsc.org/

Tung-Ming Pan,*[a] Chih-Wei Wang,[a] Wen-Hui Weng,[b] and See-Tong Pang[c]

This paper describes the impact of titanium content and postdeposition annealing on the structural properties and sensing characteristics of $TbTi_xO_y$ sensing membranes deposited on Si substrates through reactive co-sputtering. X-ray diffraction, atomic force microscopy, secondary ion mass spectrometry, and X-ray photoelectron spectroscopy were used to study the structural, morphological and chemical features of these films as functions of the growth conditions (Ti plasma powers of 80 W, 100 W, and 120 W; temperatures ranging from 700 to 900 °C). The observed structural properties were then correlated with the resulting pH sensing performances. The $TbTi_xO_y$ electrolyte-insulator-semiconductor device prepared under a Ti plasma condition of 100 W with subsequent annealing at 900 °C exhibited the best sensing characteristics, including pH sensitivity, hysteresis and drift. We attribute this behaviour to the optimal titanium content and annealing temperature in this oxide film forming a well-crystallized $Tb_2Ti_2O_7$ structure and a smoother surface.

Introduction

Medical industry, food quality evaluation and food monitoring are responsible for the increasing research and development in the field of biosensors.[1] In this field, ion sensitive field-effect transistors (ISFETs) have been investigated since they have advantages such as small size, robustness, rapid response, and low output impedance, in addition to be compatible with metal-oxide-semiconductor (CMOS) process. The concept of an ISFET device is based on the metal-oxide-semiconductor field-effect transistor (MOSFET) operating theory, where metal gate electrode is removed and replaced by an electrolytic solution and a reference electrode. Compared with such an ISFET device, the main advantage of an electrolyte-insulator-semiconductor (EIS) sensor is its simple structure and fabrication process. The investigation of an insulator material is one of the most important parts of the process, because it has no the metal gate electrode to directly immerse in a buffer solution. Consequently, the insulator material will be responsible for the detection of the biological and chemical specimens because the change in the pH and electrolyte concentration induces the change in the electrolyte–insulator surface potential, thereby causing alterations in the channel conductance and current modulation.[2]

[a]*Department of Electronics Engineering, Chang Gung University, Taoyuan 333, Taiwan.*
[b]*Department of Chemical Engineering & Biotechnology, Institute of Biotechnology, National Taipei University of Technology, Taipei 112, Taiwan.*
[c]*Division of Urology, Chang Gung Memorial Hospital, Taiyuan 333, Taiwan.*
**Corresponding author: Dr. Tung-Ming Pan ;Fax: +886-3-2118507 Tel: +886-3-2118800 Ext. 3349;E-mail: tmpan@mail.cgu.edu.tw*

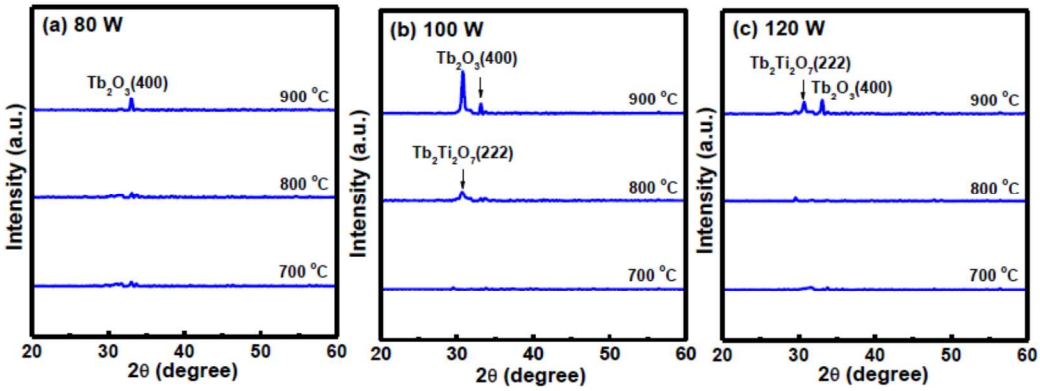

Fig. 1 XRD patterns of $TbTi_xO_y$ films prepared under Ti plasma power conditions of (a) 80 W, (b) 100 W, and (c) 120 W with subsequent annealing at various temperatures.

As a result of the reduction in gate leakage and the increase in gate capacitance density, high-κ materials currently emerges as one of the most promising candidates to be implemented in the gate dielectrics of CMOS processes.[3] However, the oxygen vacancies of high-κ dielectrics cause a relative high density of traps in the bulk and at the interface of dielectric stacks.[4] Besides, there is a problem of the formation of interfacial oxides, silicates and silicides at the oxide/Si interface arising from the film deposition or the subsequent rapid thermal annealing (RTA).[4-5] Various high-κ gate dielectric materials, such as Al_2O_3, Ta_2O_5, ZrO_2, and Gd_2O_3,[6-9] can be employed for achieving a pH response in the ISFET or EIS device. The pH sensitivity of ISFET or EIS devices depends mainly on the choice of the gate dielectric material. Recently, rare-earth (RE) oxide materials, including Pr_2O_3, Sm_2O_3, Er_2O_3, and Lu_2O_3,[10-12] are attractive candidates for alternative gate dielectrics based on thermodynamic considerations, their moderately high dielectric constants, and their high conduction band offsets. Kitai[13] also reported that terbium oxide (Tb_4O_7) thin film possesses desirable properties for use in CMOS devices, including a high dielectric constant and a low leakage current. Nevertheless, the technical problems of using an RE oxide film as the sensing membrane are the oxygen vacancies and moisture absorption,[14] which both affect the sensing performance. These technical issues can be solve through the incorporation of Ti or TiO_x in the RE oxide film, leading to lower reactivity toward water, thinner interfacial layers, higher capacitance, and lower leakage currents characteristics[15-17] that are valuable when EIS sensing devices for the detection of ions or molecules in aqueous solutions. In addition to the aforementioned RE oxide materials, terbium oxide (TbO_x) is another potential material for fabricating the sensing membrane in an EIS device; it features an appropriate lattice compatible with silicon, good thermal stability in the presence of silicon, and large conduction and valence band offsets.[12] However, experimental data related to the effects of titanium content in the $TbTi_xO_y$ sensing membranes is rarely investigated. In this study, we describe the effect of the Ti atom content in the $TbTi_xO_y$ films deposited on a Si substrate through reactive co-sputtering and subsequent post-deposition annealing (PDA) at various temperatures. We used X-ray diffraction (XRD), atomic force microscopy (AFM), secondary ion mass spectrometry (SIMS) and X-ray photoelectron spectroscopy (XPS) to examine the structures, surface roughnesses, elemental depth profiles, and compositions, respectively, of the $TbTi_xO_y$ films annealed at various temperatures. Furthermore, we correlated the observed structural and surface properties of the $TbTi_xO_y$ sensing membranes with their resultant pH sensing performances, measured in terms of detection sensitivity, hysteresis, and signal drifting.

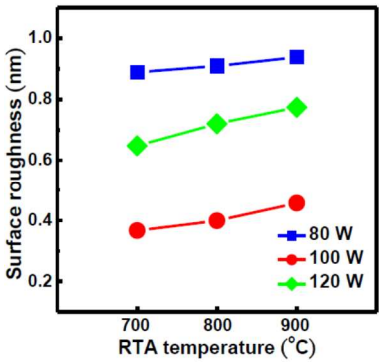

Fig. 2 Surface roughness of the $TbTi_xO_y$ films plotted as a function of the RTA temperature for each of the Ti plasma power conditions.

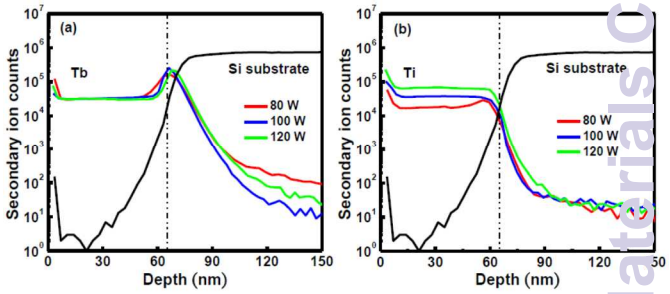

Fig. 3 SIMS profiles of (a) terbium and (b) titanium in $TbTi_xO_y$ films prepared under different Ti power conditions.

Experimental

The EIS sensor structure with $TbTi_xO_y$ sensing membranes was fabricated on a 4-in p-type (100) silicon wafer. Before deposition of these membranes, the wafer was cleaned using a standard RCA process and then they were treated with 1% HF. A film (~60 nm) of $TbTi_xO_y$ was deposited on the Si substrate through reactive co-sputtering using Tb and Ti as targets in a diluted O_2 ambient. The co-sputtering plasma power conditions were the Tb of 100 W and Ti of 80, 100, and 120 W. The deposited time of the sputtering under Ti plasma power of 80, 100, and 120 W was ~50, 45, and 40 min, respectively. Subsequently, all of the samples were annealed in a lamp-based

RTA at different temperatures (700, 800, 900 °C) under ambient O_2 conditions for 30 s. The backside contact (a 400-nm-thick Al film) of the Si wafer was deposited using a thermal coater. The sensing zone on the deposited $TbTi_xO_y$ films was then defined by a standard photolithography process using SU8-2005 (MicroChem, USA) as a photoresist, followed by assembly of the EIS structures on the copper line of a custom-made printed circuit board (PCB), using a silver gel to form the conductive line. A hand-made epoxy package was used to encapsulate the EIS structure from the Cu line.

The film structure of the $TbTi_xO_y$ films annealed at different temperatures (700, 800, 900 °C) was investigated through a Bruker-AXS D5005 diffractometer (XRD). The surface morphology and roughness of the films were studied by using an NT-MDT Solver P47 (AFM). The elemental depth profiles of terbium and titanium in $TbTi_xO_y$ films were analyzed using a Cameca IMS 4F SIMS instrument. The composition and chemical bonding in each $TbTi_xO_y$ film were explored using a Physical Electronics Quantum 2000 XPS instrument. The pH sensing performance of the $TbTi_xO_y$ EIS sensors was evaluated using standard buffer solutions having values of pH ranging from 2 to 12. For a given experiment, each pH condition was tested in triplicate. The capacitance–voltage (C–V) curves for the EIS devices in the standard buffer solutions at different values of pH were then measured through a commercial Ag/AgCl glass reference electrode using a Hewlett–Packard (HP) 4284A LCR meter. To avoid any interference caused by ambient light, all of the experimental setups were kept in the dark and performed at room temperature.

Results and Discussion

A. Structural properties of $TbTi_xO_y$ films

In this study, we explored the structures, surface roughnesses, and compositions of $TbTi_xO_y$ sensing membranes fabricated various Ti power conditions and then annealed at 700, 800, and 900 °C. We used XRD to analyse the crystalline structures of the $TbTi_xO_y$ sensing membranes prepared under the various Ti plasma powers and then annealed at different temperatures. Fig. 1 reveals that the intensities and orientations of the diffraction peaks of the studied $TbTi_xO_y$ films as a function of the PDA temperature for each of the three Ti power conditions. For the sample annealed at 700 °C, no diffraction peak (or relatively weak peak) was observed in the XRD patterns, indicating an amorphous structure. The intensity of diffraction peak increases with increasing the PDA temperature. After annealing at 900 °C, only one weak Tb_2O_3 (400) diffraction peak appeared for the sample prepared at a Ti plasma condition of 80 W, as shown in Fig. 1(a). This result may be attributed to an amorphous $TbTi_xO_y$ structure with a low Ti content. Moreover, Fig. 1(b) depicts that the $Tb_2Ti_2O_7$ (222) peak became stronger than the Tb_2O_3 (400) peak in the spectrum of the sample prepared under the 100 W condition, suggesting a well-crystallized $Tb_2Ti_2O_7$ film. The crystal structure of $Tb_2Ti_2O_7$ film is face-centered cubic. The sample prepared under the 120 W condition and then annealed at 900 °C exhibited Tb_2O_3 (004) and $Tb_2Ti_2O_7$ (222) peaks, as shown in Fig. 1(c).

In addition to this structural investigation, we also used AFM to explore the impact of the titanium content and thermal annealing temperature on the surface roughnesses of the $TbTi_xO_y$ sensing membranes. Fig. 2 depicts the surface roughness of the $TbTi_xO_y$ films as a function of the RTA temperature for each of the three Ti power conditions. The film

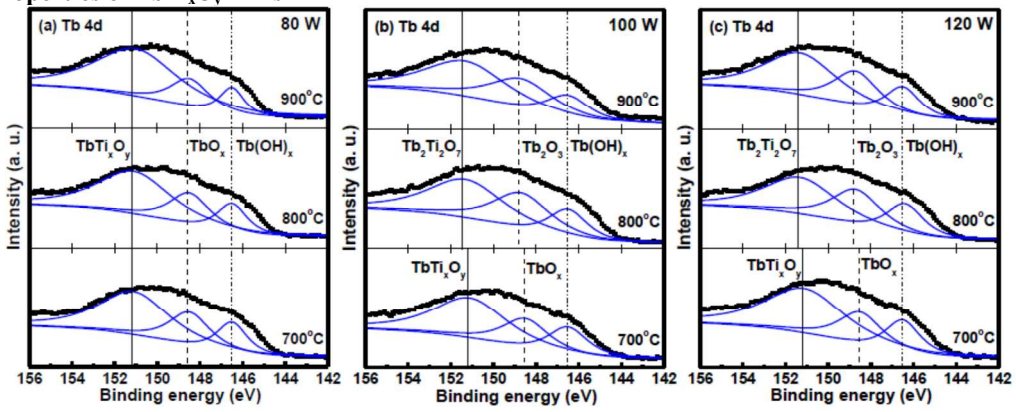

Fig. 4 Tb $4d_{5/2}$ XPS spectra of $TbTi_xO_y$ films prepared under Ti plasma power conditions of (a) 80 W, (b) 100 W, and (c) 120 W with subsequent annealing at various temperatures.

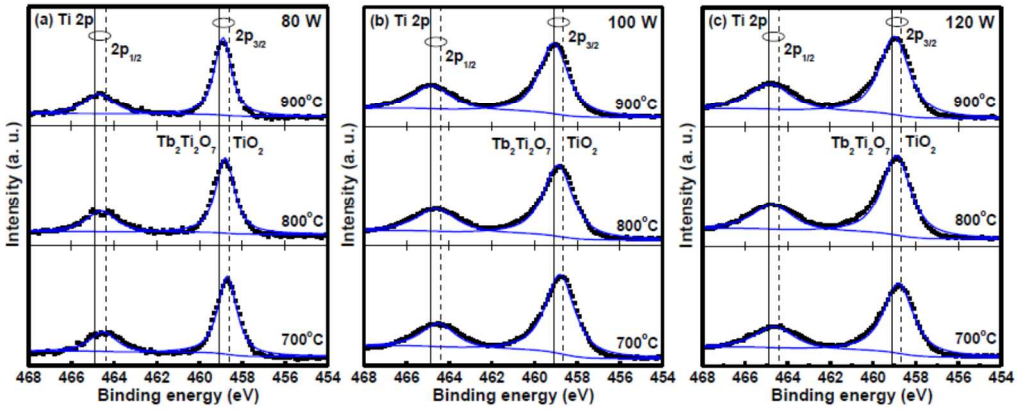

Fig. 5 Ti 2p XPS spectra of $TbTi_xO_y$ films prepared under Ti plasma power conditions of (a) 80 W, (b) 100 W, and (c) 120 W with subsequent annealing at various temperatures.

prepared under the 80 W condition exhibited a larger surface roughness than other conditions. The larger surface roughness may be attributed to the moisture absorption of Tb_2O_3 due to the presence of a low Ti content in the $TbTi_xO_y$ film producing more Tb_2O_3 components, leading to the nonuniform volume expansion of the film.[13] In contrast, the $TbTi_xO_y$ film prepared at a Ti plasma condition of 100 W exhibits the lowest surface roughness among these plasma conditions. This result may be due to the optimal titanium content in the film forming a well-crystallized $Tb_2Ti_2O_7$ structure, thus suppressing the moisture absorption. In addition, the surface roughness clearly increased with increasing the RTA temperature. We suggest that this behaviour is due to an increased number of Ti and Tb atoms in the film increasing the clustering of grains, thereby increasing the surface roughness of the $TbTi_xO_y$ film.

SIMS depth profiles of the Tb and Ti atoms for $TbTi_xO_y$ films annealed at 900 °C as a function of the Ti plasma condition are shown in Fig. 3(a) and (b), respectively. The samples prepared under three Ti plasma powers had the same level of terbium. In addition, we found that the film at the interface between the oxide and Si substrate exhibited the highest level of terbium. This result may be attributed to the formation of a nonstoichiometric silicate layer during high-temperature annealing.[12] In contrast, the level of titanium clearly increased with increasing the Ti plasma power. For the sample prepared under the 100 W condition, the level of titanium in the bulk was almost the same as that of terbium.

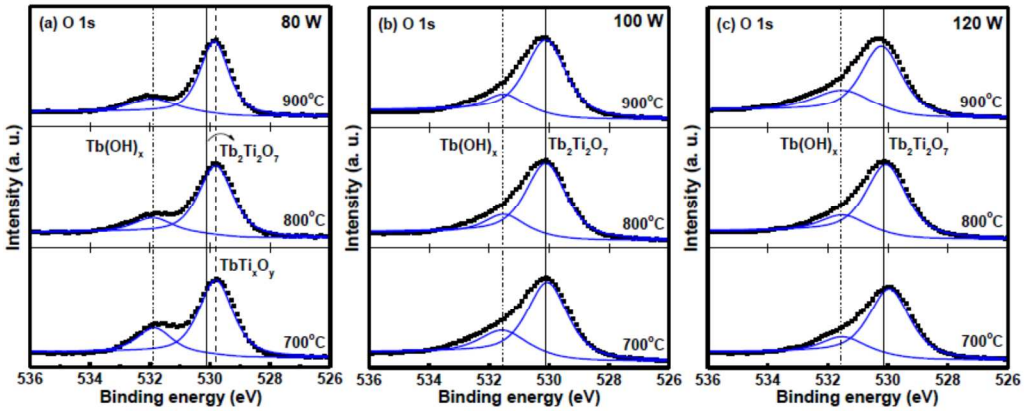

Fig. 6 O 1s XPS spectra of $TbTi_xO_y$ films prepared under Ti plasma power conditions of (a) 80 W, (b) 100 W, and (c) 120 W with subsequent annealing at various temperatures.

We used XPS to examine the structural and compositional changes in the $TbTi_xO_y$ films as functions of both the Ti plasma power conditions and the annealing temperatures. A multipeak Lorentzian-Gaussian deconvolution procedure was used to extract the exact line positions and intensities. When peak fitting was necessary to locate peak position or integrate area, Lorentzian-Gaussian functions were produced by minimizing the misfit error. Fig. 4 (a)-(c) show the Tb $4d_{5/2}$ energy level region in the XPS spectra of the samples after PDA at different temperatures, with their appropriate peak curve-fitting lines corresponding to chemical states. Under the 80 W condition, the Tb $4d_{5/2}$ signal comprised of three peaks at 151.2, 148.6, and 146.5 eV, as shown in Fig. 4(a), which we assign to $TbTi_xO_y$, TbO_x, and $Tb(OH)_x$, respectively. The chemical structure of Tb-O in $Tb_2Ti_2O_7$ is similar to Tb_2O_3 (148.8 eV)[18] with trivalent Tb ions (Tb^{3+}) rather than TbO_2 (149.2 eV)[19] with tetravalent Tb ions (Tb^{4+}). The peak intensities of TbO_x and $Tb(OH)_x$ decreased upon increasing the RTA temperature, whereas that of $TbTi_xO_y$ increased upon increasing the RTA temperature. In contrast, under both the 100 and 120 W conditions, the Tb $4d_{5/2}$ signal of the sample annealed at 700 °C also had three peaks: one peak at 151.2 eV ($TbTi_xO_y$), another peak at 148.6 eV (TbO_x), and the other peak at 146.5 eV, while the sample after RTA at 800 and 900 °C comprised of three peaks: one peak for $Tb_2Ti_2O_7$ at 151.4 eV, another peak for Tb_2O_3 at 148.8 eV[18], and the other peak for $Tb(OH)_x$ at 146.5 eV. The Tb $4d_{5/2}$ peak position at 151.4 eV for the $Tb_2Ti_2O_7$ film had shifted by about 0.2 eV relative to that of the $TbTi_xO_y$ film. We attribute this behaviour to the reactions of the Ti with Tb and O atoms to form a $Tb_2Ti_2O_7$ structure. The intensity of the Tb $4d_{5/2}$ peak corresponding to Tb_2O_3 and $Tb(OH)_x$ for the film annealed at 900 °C is lower than that at 800 °C, whereas that corresponding to $Tb_2Ti_2O_7$ for the sample annealed at 900 °C is higher compared to 800 °C, as shown in Fig. 4(b) and (c). These results suggest that a higher reaction degree of the titanium with terbium and oxygen atoms resulting in the formation of a well-crystallized $Tb_2Ti_2O_7$ film.

Fig. 5(a)-(c) show the variation in the Ti 2p split peaks as functions of both the Ti plasma conditions and the annealing temperatures. The split peaks for the Ti $2p_{1/2}$ and $2p_{3/2}$ energy levels at 464.3 and 458.7 eV, respectively, were assigned to TiO_2.[16] Under each of the three Ti plasma conditions, the shift of the Ti split peak positions toward higher binding energy occurred upon increasing the annealing temperature, indicating the formation of Tb–O–Ti bonds. When annealing was performed at 900 °C, the Ti 2p split peaks shifted to higher binding energy by about 0.3–0.5 eV relative to the TiO_2 position. This change in the Ti bonding status reflected the formation of a better $Tb_2Ti_2O_7$ structure.

Fig. 6(a)-(c) display the O atom binding energy region of the XPS spectra, with their appropriate peak curve-fitting lines, of the $TbTi_xO_y$ films prepared under the three Ti plasma conditions and then annealed at different temperatures. The film performed under the 80 W condition, the O 1s peak at 531.9 eV represents the Tb–$(OH)_x$ bond, whereas the O 1s peak at 529.8 eV is assigned to the Tb–O–Ti ($TbTi_xO_y$) bond. The O 1s peak intensity corresponding to $Tb(OH)_x$ decreased upon increasing the RTA temperature, as shown in Fig. 6(a). This outcome may be attributed to higher-temperature annealing increased the film condensation and reduced the oxygen vacancies in the film, thus resulting in the formation of a thinner $Tb(OH)_x$ layer. The O 1s spectra in Fig. 6(b) can be deconvoluted to two chemical states: the high binding energy state at 531.5 eV can be related to O atoms in $Tb(OH)_x$ and the low binding energy state at 530.1 eV (530 eV for sample

annealed at 700 °C) to O atoms in the $Tb_2Ti_2O_7$ ($TbTi_xO_y$). The intensity of the O 1s peak corresponding to $Tb(OH)_x$ decreased upon increasing the RTA temperature, whereas that corresponding to $Tb_2Ti_2O_7$ increased, accordingly. The strong resistance to the moisture of $TbTi_xO_y$ film may be due to the formation of a better $Tb_2Ti_2O_7$ structure during high-temperature annealing. Under the 120 W condition, the fitted O 1s peaks at 529.9, 530, and 530.2 eV represent the $TbTi_xO_y$, as shown in Fig. 6(c). Furthermore, the shift of the O 1s peak to a higher binding energy increases upon increasing the RTA temperature, suggesting a high Ti content in the $TbTi_xO_y$ film.

B. Sensing characteristics of $TbTi_xO_y$ EIS devices

The operation mechanism of an ISFET or EIS device is explained using the site-binding model.[20] When the gate oxide is immersed to the tested solution, the surface potential (ψ_0) in the silicon channel is changed by the binding of H^+ ions onto the surface of gate oxide. The pH sensitivity is generally determined by the number of binding sites that exist on the surface of the gate oxide. Based on this model, the existence of ions in the solution react with positively or negatively charged active sites at the oxide surface creating hydrogen-active site pairs, and thereby changing the total value of the active site charge at the oxide surface. This, in turn, changes the channel current of such an ISFET device through the variation of the threshold voltage. According to the Gouy–Chapman–Stern theory,[21] the gradient of ion concentration is created in the electrolyte due to the binding of the ions with the active sites. Consequently, the double layer is established at the electrolyte–oxide border. The double layer is composed of the Helmholtz layer and the diffuse layer. Generally, the Helmholtz layer consists of adsorbed water species (H^+ and OH^-) at the surface of the semiconductor, followed by a layer of solvated electrolyte ions. The water species form the so-called inner Helmholtz layer, whereas the solvated ions form the external Helmholtz layer. The two Helmholtz layers can be considered to form a planar capacitor.[21] Using the Gouy–Chapman–Stern model, we can derive the surface potential[22]as:

$$\psi_0 = -\frac{2k_BT}{q} sinh^{-1}\left(\frac{\sigma_d}{\sqrt{8\varepsilon_W k_B T C_0}}\right) - \frac{\sigma_d}{C_{stern}} \quad (1)$$

where k_B is the Boltzmann constant, T is the absolute temperature, q is the elementary charge, σ_d is the charge density in the diffuse layer, ε_W is the dielectric constant of water, C_0 is the solution concentration, and C_{stern} is the Stern capacitance. The condition of charge neutrality for the structure of an EIS device gives:

$$\sigma_d + \sigma_0 + \sigma_{EIS} = 0 \quad (2)$$

where σ_0 is the charge density of the surface sites and σ_{EIS} is the charge density in the silicon substrate and the gate oxide. The gate oxide charges can be divided into the interface trapped charge, fixed oxide charge, oxide trapped charge, and mobile ionic charge. By using the site-binding model,[20] we can write the charge density as:

$$\sigma_0 = qN_s \frac{([H^+]_S)^2 - K_aK_b}{K_a[H^+]_S + ([H^+]_S)^2 + K_aK_b} = -q[B] \quad (3)$$

where N_s is the total number of available surface binding sites, K_a and K_b are the acid and base dissociation constants for the chemical reactions at the oxide interface, respectively, [B] is the number of charged groups, and $[H^+]_S$ is the surface concentration of the H^+ ions, which is related to the bulk value ($[H^+]_B$) by Boltzmann statistics:

$$[H^+]_S = [H^+]_B e^{-\frac{q\psi_0}{k_BT}} \quad (4)$$

The relationship between ψ_0 and σ_0 can be expressed as:

$$\sigma_0 = C_{DL}\psi_0 = -\sigma_{DL} \quad (5)$$

where C_{DL} is the capacitance of the double layer and σ_{DL} is the charge density of the double layer. As a result of a small change in the surface potential, the ability of the electrolyte solution to adjust the amount of stored charge is the double layer capacitance:[23]

$$\frac{\partial\sigma_0}{\partial\psi_0} = -\frac{\partial\sigma_{DL}}{\partial\psi_0} = C_{DL} \quad (6)$$

The surface charge density of oxide can be modulated by the variation in the H^+ ion concentration at the interface:

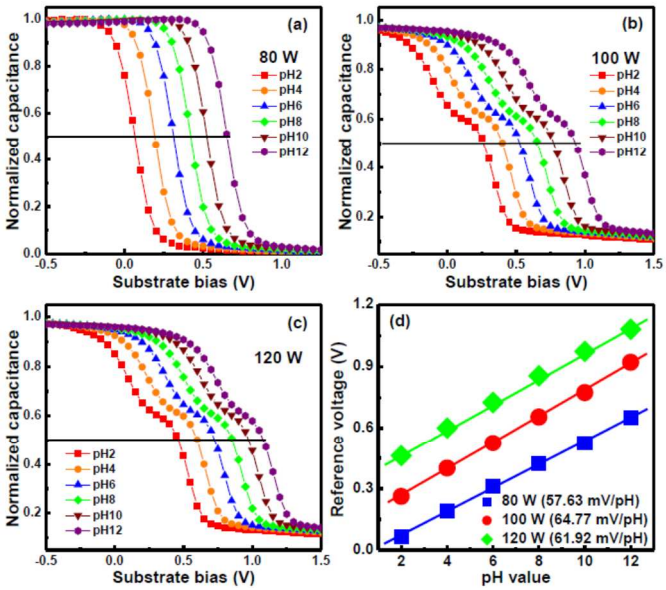

$$\frac{\partial\sigma_0}{\partial pH_S} = -q\frac{\partial[B]}{\partial pH_S} = -qN_s\frac{K_a([H^+]_S)^2 + 4[H^+]_S K_aK_b + (K_a)^2K_b}{[K_a[H^+]_S + ([H^+]_S)^2 + K_aK_b]^2} = -q\beta_{int} \quad (7)$$

where β_{int} is the capability to buffer small changes in the surface pH (pH_S), but not in the pH solution (pH_B). Combination of (6) and (7) results in an expression for the sensitivity of the surface potential towards the change in pH_S:

$$\frac{\partial\psi_0}{\partial pH_S} = \frac{\partial\psi_0}{\partial\sigma_0}\frac{\partial\sigma_0}{\partial pH_S} = -\frac{q\beta_{int}}{C_{DL}} \quad (8)$$

The static behaviour of an EIS device is derived by taking into account the potential differences among the interfaces. In this way the following expression for the flatband voltage (V_{FB}) is obtained:[23]

$$V_{FB} = E_{ref} - \psi_0 + \chi^{sol} - \frac{\Phi_{Si}}{q} - \frac{Q_{ss}}{C_{ox}} \quad (9)$$

where E_{ref} is the potential of the reference electrode (Ag/AgCl here considered), χ_{sol} is the electrolyte-insulator surface dipole potential, Φ_{Si} is the silicon workfunction, Q_{ss} is the fixed surface-state charge density at the insulator-semiconductor interface, and C_{ox} is the gate oxide capacitance. In this equation, all terms are constant except for ψ_0, ψ_0 can control the

Fig. 7 (a) C–V curves response for $TbTi_xO_y$ EIS devices prepared under Ti plasma power conditions of (a) 80 W, (b) 100 W, and (c) 120 W and then annealed at 900 °C, when inserted into solution with pH 7. (d) Reference voltage plotted as a function of pH for $TbTi_xO_y$ EIS devices fabricated different Ti power conditions, measured at room temperature.

dissociation of the oxide surface groups, causing the variation in the electrolyte pH of an EIS device.

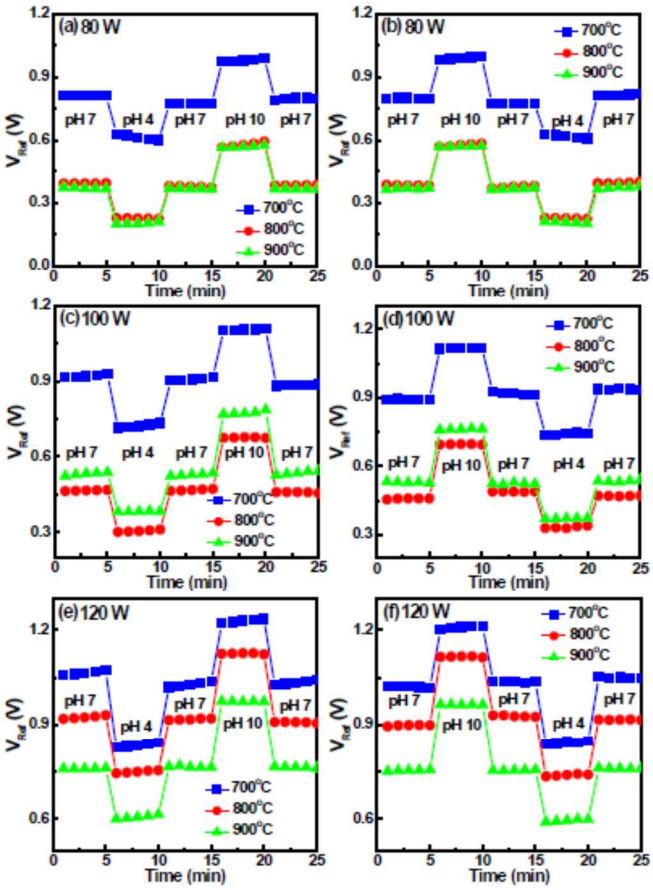

Fig. 9 Drift phenomena as a function of pH for $TbTi_xO_y$ EIS devices prepared under Ti plasma power conditions of (a) 80 W, (b) 100 W, and (c) 120 W and then annealed at different temperatures.

Fig. 8 Hysteresis characteristics as a function of pH for $TbTi_xO_y$ EIS devices prepared under Ti plasma power conditions of (a, b) 80 W, (c, d) 100 W, and (e, f) 120 W and then annealed at different temperatures, during the loops of pH 7→4→7→10→7 and pH 7→10→7→4→7, respectively.

The pH sensitivity of such an EIS device is generally determined by the change in the flatband voltage per pH change in the tested solution. The pH sensitivity of the $TbTi_xO_y$ sensing membranes can be described using the combination of the site-binding model and the double layer theory of Gouy–Chapman–Stern model to explain the ionic absorption processes at the electrolyte/oxide interface. The surface of an oxide film contains a large amount of unsatisfied bonds. In the absence of specific adsorption, the only ions capable of making bonds with these sites are the hydrogen and hydroxyl ions. According to the equation (8) and (9), the change of H^+ ion concentration (pH_S) induces the variation in the ψ_0 and thus modulates the β_{int}. This β_{int} value is related to mainly the surface reactivity (i.e. surface site density). Based on the above equations, it can be supposed that the higher N_s (or the higher β_{int}) accordingly contributes to a higher sensitivity and also the more linear response of pH detection. To evaluate the pH sensing performance of the $TbTi_xO_y$ EIS sensors, we examined their behaviour toward standard buffer solutions having values of pH ranging from 2 to 12. Fig. 7(a)-(c) depict the C–V curves of the

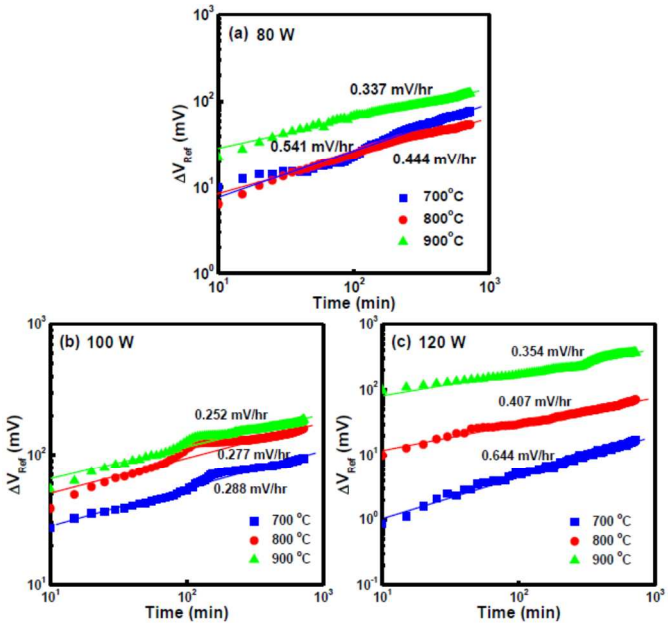

$TbTi_xO_y$ EIS sensors prepared under three Ti plasma conditions and then annealed at 900 °C. The EIS sensor under both 100 and 120 W conditions provided distorted C–V curves, as has been reported in the literature,[24] presumably due to the presence of interfacial traps in the oxide. In EIS pH sensing, a change in pH normally causes a flatband voltage shift of the C–V curves, mainly due to ionization of the surface OH groups by H^+ or OH^- ions,[23] in turn modifying the surface potential through dipole formation on the sensing membrane. Moreover, Fig. 7(d) presents the V_{REF} of the $TbTi_xO_y$ EIS sensors prepared under three plasma power conditions as a function of pH. Here, the reference voltages were determined from the obtained C–V curves at a normalized capacitance of 0.5.[24] This EIS-based pH sensor exhibited a linear response upon increasing the pH from 2 to 12. It is found that the $TbTi_xO_y$ EIS sensor prepared under the 100 W condition exhibited a better sensitivity of 64.77 mV/pH than those of the devices. This result could be attributed to the higher N_s in the $TbTi_xO_y$ film. To determine the pH detection sensitivities of the $TbTi_xO_y$ sensing membranes that had been subjected to various annealing temperatures, we recorded their C–V curves and then evaluated them based on the approach described above. The $TbTi_xO_y$ EIS device annealed at 900 °C exhibited the best pH detection sensitivity than other temperatures (700 and 800 °C), presumably because this annealing temperature led to the formation of a well-crystallized $Tb_2Ti_2O_7$ structure, consistent with the results in figure 1. As a whole, the $TbTi_xO_y$ films explored in this study demonstrated pH detection sensitivity superior to those of materials commonly used for ISFET- and EIS-based sensing, namely Al_2O_3 (54–56 mV/pH)[25], Ta_2O_5 (56–58 mV/pH)[25], ZnO_2 (58 mV/pH)[26], ZrO_2 (58.7 mV/pH)[8], Lu_2O_3 (56 mV/pH)[27], Nd_2TiO_5 (57 mV/pH)[28], and Sm_2TiO_5 (61 mV/pH)[24].

Besides the sensitivity detection, hysteresis and drift phenomena are two other critical performance features affecting the success of a sensing device. The slow response and hysteresis behaviour can be interpreted in terms of a surface-site model,[29] in which a portion of the surface sites reacts very slowly. Hysteresis characteristics can occur due to defects in a

sensing membrane, leading to the formation of porous structures.[7,30] The interior sites of these porous defects can react with ions present in the solution, thus causing a hysteresis response. Another possible cause is the interaction of the ions in the solution with the responding sites along the boundaries of grains on the sensing membrane.[7,30] In this study, we evaluated the hysteresis behaviour of $TbTi_xO_y$ EIS sensor devices prepared under three Ti plasma powers and then annealed at different temperatures, as shown in Fig. 8(a)-(f), directly immersed in each pH standard solution for up to 1500 s in two set cycles of pH 7→4→7→10→7 and pH 7→10→7→4→7. The hysteresis voltage is defined herein as the difference between the initial and terminal reference voltages measured in this cycle. We found that the $TbTi_xO_y$ EIS sensor fabricated under 100 W condition and annealed at 900 °C had the lowest hysteresis voltage (~3 and 5 mV) for pH loops of 7→4→7→10→7 and 7→10→7→4→7 among the systems studied herein, presumably suggesting the formation of a smoother surface and a well-crystallized $Tb_2Ti_2O_7$ structure, causing a lower number of crystal defects in the sensing membrane. In contrast, the sample annealed at 700 °C exhibited the highest hysteresis voltage (15~44 mV) during pH loops of 7→4→7→10→7 and 7→10→7→4→7, indicating a higher density of crystal defects in its $TbTi_xO_y$ sensing membrane.

Furthermore, we also evaluated the drift rate of the pH sensing by measuring the change in the reference voltage after submerging the EIS device in a standard buffer solution at pH 7 for up to 12 h. The drift of an EIS sensor can be explained by a hopping and/or trap-limited transport mechanism[31,32] to determine the rate of hydration of the gate oxide. The change in the reference voltage can be described as $\Delta V_{Ref}=V_{Ref}(t)-V_{Ref}(0)$. The drift phenomenon of an ISFET or EIS pH sensor is related to the penetration of ions from the electrolytes into the sensing membrane.[33] Charged electrolytes can penetrate the hydrated layer of a sensing membrane to cause a decrease in the effective gate oxide thickness.[7] The change in gate capacitance induces non-ideal effects during ISFET or EIS pH sensing. Figure 9(a)-(c) demonstrate the drift characteristics of $TbTi_xO_y$ EIS sensors prepared under different plasma power conditions and then annealed at various temperatures; here, the slope of the reference voltage deviation reflects the stability of the EIS sensor. The $TbTi_xO_y$ EIS device fabricated under the 100 W condition and annealed at 900 °C exhibited the greatest long-term stability (slope = 0.252 mV/h) in comparison with the other studied systems. The lower drift rate for the film annealed at the highest temperature might be due to its lower level of crystal defects and smoother surface, leading to lower ionic mobility. The hysteresis voltage and drift rate of $TbTi_xO_y$ sensing membrane are comparable to other sensing membranes such as Al_2O_3 (3 mV and < 0.1 mV/h)[34], WO_3 (7.2 mV and 15.7 mV/h)[35], RuO_2 (2.2 mV and 0.38 mV/h)[36], Lu_2O_3 (2.2 mV and 1.32 mV/h)[27], Nd_2TiO_5 (2.3 mV and 1.8 mV/h)[28], and Sm_2TiO_5 (2.7 mV and 1.11 mV/h)[24].

Conclusions

In this study, we fabricated $TbTi_xO_y$ sensing membranes deposited on Si substrates through reactive cosputtering under three Ti plasma power conditions and subsequent annealing at various temperatures. The effect of titanium content and PDA on the structural and surface properties of the $TbTi_xO_y$ sensing membrane as well as on the pH sensing performance of the corresponding EIS sensors was investigated. The $TbTi_xO_y$ EIS sensor fabricated under the 100 W condition with subsequent annealing at 900 °C exhibited a high pH sensitivity of 64.77 mV/pH, a small hysteresis voltage of ~3 mV and a low drift rate of 0.252 mV/h. We attribute this high performance to the formation of a well-crystallized $Tb_2Ti_2O_7$ structure and a smoother surface at this condition. The EIS device incorporating a $TbTi_xO_y$ sensing membrane appears to be a very promising sensing membrane for use in the field of electrochemical sensors and bioelectronic devices.

Acknowledgement

The authors thank the Chang Gung Memorial Hospital and the National Science Council of the Republic of China, Taiwan, for financially supporting this research under contracts of CMRPD2C0151 and NSC 98-2221-E-182-056-MY3, respectively.

References

1 A. D. Barros, K. F. Albertin, J. Miyoshi, I. Doi, and J. A. Diniz, Microelectron. Eng., 2010, **87**, 443.
2 P. Bergveld, Sens. Actuators B, 2003, **88**, 1.
3 G. D. Wilk, R. M. Wallace, and J. M. Anthony, J. Appl. Phys., 2001, **89**, 5243.
4 E. Gusev, *Defects in High-k Gate Dielectrics Stacks*, Springer, Dordrecht, 2006.
5 M. Houssa, *High-k Gate Dielectrics*, Institute of Physics, Bristol, 2004.
6 T. Matsuo, M. Esashi, and H. Abe, IEEE Trans. Electron Devices, 1979, **26**, 1856.
7 L. Bousse, S. Mostarshed, B. van der Schoot, and N. F. de Rooij, Sens. Actuators B, 1994, **17**, 157.
8 K. M. Chang, C. T. Chang, K. Y. Chao, and C. H. Lin, Sensors, 2010, **10**, 4643.
9 J. L. Her, M. H. Wu, Y. B. Peng, T. M. Pan, W. H. Weng, S. T. Pang, and L. Chi, Int. J. Electrochem. Sci., 2013, **8**, 606.
10 O. Engstrom, B. Raeissi, S. Hall, O. Buiu, M. C. Lemme, H. D. B. Gottlob, P. K. Hurley, and K. Cherkaoui, Solid-State Electron., 2007, **51**, 622.
11 J. Paivasaari, M. Putkonen, and L. Niinistf, Thin Solid Films, 2005, **472**, 275.
12 M. Fanciulli and G. Scarel, *Rare Earth Oxide Thin Film: Growth, Characterization, and Applications*, Springer, Berlin, 2007.
13 S. Kitai, O. Maida, T. Kanashima, and M. Okuyama, Jpn. J. Appl. Phys., 2003, **42**, 247.
14 Y. Zhao, K. Kita, K. Kyuno, and A. Toriumi, Appl. Phys. Lett., 2006, **89**, 252905.
15 S. Jeon and H. Hwang, Appl. Phys. Lett., 2002, **81**, 4856.
16 T. Schroeder, G. Lupina, J. Dabrowski, A. Mane, Ch. Wenger, G. Lippert, and H. J. Mussig, Appl. Phys. Lett., 2005, **87**, 022902.
17 T. M. Pan, W. H. Shu, and J. L. Hong, Appl. Phys. Lett., 2007, **90**, 222906.
18 Y. Uwamino, T. Ishizuka, and H. Yamatera, J. Electron Spectrosc. Relat. Phenom., 1984, **34**, 67.
19 D. D. Sarma and C. N. R. Rao, J. Electron Spectrosc. Relat. Phenom., 1980, **20**, 25.

20 R. E. G. van Hal, J. C. T. Eijkel, and P. Bergveld, Sens. Actuators B, 1995, **24-25**, 201.
21 M. W. Shinwari, M. J. Deen, and D. Landheer, Microelectron. Reliab., 2007, **47**, 2025.
22 L. Bousse, N. F. De Rooij, and P. Bergveld, IEEE Trans.Electron Devices, 1983, **30**, 1263.
23 P. Bergveld and A. Sibbald, *Comprehensive Analytical Chemistry. v. 23. Analytical and Biomedical Applications of Ion-Selective Field-Effect Transistors*, Elsevier Science Publishing Company Inc, New York, 1988.
24 M. H. Wu, T. W. Lin, M. D. Huang, H. Y. Wang, and T. M. Pan, Sens. Actuators B, 2010, **146**, 342.
25 Y. Miao, J. Guan, and J. Chen, Biotechnol. Adv., 2003, **21**, 527.
26 C. W. Liao, J. C. Chou, T. P. Sun, S. K. Hsiung, and J. H. Hsieh, Sens. Actuators B, 2007, **123**, 720.
27 T. M. Pan and C. W. Lin, J. Electrochem. Soc., 2011, **158**, J96.
28 T. M. Pan, J. C. Lin, M. H. Wu, and C. S. Lai, Biosens. Bioelectron., 2009, **24**, 2864.
29 L. Bousse, D. Hafeman, and N. Tran, Sens. Actuators B, 1990, **1**, 361.
30 L. Bousse, H. H. van den Vlekkert, and N. F. de Rooij, Sens. Actuators B, 1990, **2**, 103.
31 H. Scher and E. W. Montroll, Phys. Rev. B, 1975, **12**, 2455.
32 G. Pfister and H. Scher, Phys. Rev. B, 1977, **15**, 2062.
33 S. Jamasb, S. D. Collins, and R. L. Smith, IEEE Trans. Electron Devices, 1998, **45**, 1239.
34 M. J. Schoning, Y. G. Mourzina, J. Schubert, W. Zander, A. Legin, Y. G. Vlasov, and H. Luth, Sens. Actuators B, 2001, **78**, 273.
35 J. L. Chiang, S. S. Jan, J. C. Chou, and Y. C. Chen, Sens. Actuators B, 2001, **76**, 624.
36 Y. H. Liao and J. C. Chou, Sens. Actuators B, 2008, **128**, 603.